Chemical Engineering Journal 451 (2023) 139077

Contents lists available at ScienceDirect

Chemical Engineering Journal

journal homepage: www.elsevier.com/locate/cej

Flexible and highly piezoelectric nanofibers with organic–inorganic coaxial structure for self-powered physiological multimodal sensing

Xingyi Wan [a,b], Zhuo Wang [a], Xinyang Zhao [a], Quanhong Hu [a,c], Zhou Li [a,b], Zhong Lin Wang [a,b,d,*], Linlin Li [a,b,c,*]

[a] Beijing Institute of Nanoenergy and Nanosystems, Chinese Academy for Sciences, Beijing 101400, PR China
[b] School of Nanoscience and Technology, University of Chinese Academy of Sciences, Beijing 100049, PR China
[c] School of Chemistry and Chemical Engineering, Guangxi University, Nanning 530004, PR China
[d] School of Materials Science and Engineering, Georgia Institute of Technology, Atlanta, GA 30332-0245, USA

ARTICLE INFO

Keywords:
$BaTiO_3$ nanowire
Coaxial structure
Interfacial coupling
Flexible piezoelectric nanogenerator
Physiological multimodal sensing

ABSTRACT

The relatively low sensitivity of flexible piezoelectric nanogenerators (PENG) is the most urgent problem to be solved for their applications in internet of things and artificial intelligences. To improve the piezoelectricity of polymeric fibers without discount of flexibility, $BaTiO_3$ nanowire (BTNW) with high aspect ratio is introduced into the piezoelectric P(VDF-TrFE) (denoted as PT) electrospun fibers to form coaxial composite nanofibers for improving the sensitivity towards external mechanical loads. To reinforce the organic–inorganic interfacial interaction for the improvement of the piezoelectric response, a nanolayer of polydopamine (PDA) is uniformly coated on the surface of BTNW (denoted as pBTNW) to form PT/pBTNW nanofibers. The introduction of 7 wt% pBTNW into the fibers significantly improves the polymeric β-phase conformation and mechanical properties, simultaneously, resulting in an optimal piezoelectric output of 18.2 V under an impact force of 5 N with excellent sensitivity of 4.3 V N^{-1}. Through both theoretical simulation and experimental characterization, the PT/pBTNW-based PENG exhibits a higher electrical output than the equivalent nanoparticle-based PENG. The optimized PENG sensor can be used for self-powered and sensitive biomonitoring of physiological movements, finger identification and voice recognition. Overall, this work offers a reliable method for enhancing piezoelectricity of flexible polymeric nanofiber and designing high-performance PENG for wearable fabric-based sensors.

1. Introduction

Nowadays, the booming development of flexible and wearable bioelectronics especially in the internet of things and artificial intelligence is penetratively influencing the way that people understand themselves and communicate with their surroundings [1,2]. The next-generation bioelectronics are urgently calling for the eco-friendly and sustainable power supply for distributed sensing. Among the different energy conversion pathways to harvest abundant energies from the environment and human bodies [3,4], piezoelectric nanogenerators (PENGs) have stand out due to the capability to convert tiny ambient mechanical energy into electricity through piezoelectric effect [5], which have shown potential applications in self-powered systems [6], wearable electronics [7], and sensory devices [8]. For the fabrication of PENGs, the fiber and fabric-based materials exhibit the unique wearable, breathable, and flexible properties for sensing biomechanical movements compared with films and other bulk materials [9–11]. Recently, many researchers have successfully developed fabric-based PENGs for speaker recognition [12], breath detecting [13], cardiovascular monitoring [14], self-powered sensors [6], and battery-free electrical neurostimulation [15].

For the fabrication of fabric-based PENGs, piezoelectric polymers and their copolymers such as polyvinylidene fluoride (PVDF) and its copolymer poly(vinylidene fluoride-trifluoride ethylene) (P(VDF-TrFE)) are suitable candidates with the intrinsic flexibility, ease of manufacture and high biocompatibility, compared with the rigid piezoceramic materials [16]. Unfortunately, the low piezoelectric coefficient of piezoelectric polymers is the main ceiling for sensing tiny biomechanical movement and stress [17–21]. For improving the mechano-electrical conversion capability [22–24], typical methods including micro-engineering, surface physicochemical modification, modulation of structural parameters have been carried out to enhance the output performance [25,26]. Specially, inorganic nanofillers have been

* Corresponding authors.
E-mail addresses: zhong.wang@mse.gatech.edu (Z. Lin Wang), lilinlin@binn.cas.cn (L. Li).

https://doi.org/10.1016/j.cej.2022.139077
Received 29 June 2022; Received in revised form 18 August 2022; Accepted 3 September 2022
Available online 8 September 2022

composited into the polymer matrix to enhance the piezoelectricity. Inorganic ceramics most frequently used include barium titanate nanoparticles (BTNP) [15], potassium sodium niobite (KNN) [27], and lead zirconate titanate (PZT) [28,29], or conductive materials such as reduced graphene oxide (rGO) [30,31], MXene [32], and polyaniline (PANI) [33]. However, the isotropous inorganic nanoparticles tend to downgrade the stress transfer process, and increase interfacial defects and cracks once agglomeration [34], Moreover, the mismatching of the mechanical modulus between the rigid inorganic nanoparticles and flexible polymer might induce inhomogeneity of the composite fibers as well as yield poor mechanical property due to the high surface energy, which largely limits enhancing effect on the piezoelectric output especially under bending force, and is detrimental to satisfactory performance of the corresponding PENGs [35–37]. Although several facial strategies have been reported to optimize the incorporation of nanoparticles, such as surface functionalization by couple agents [38], surfactants [39], and *in situ* polymerization from the nanoparticle surface [40], which could only partially solve the intrinsic problems for most nanoparticle fillers. Thus, it is highly required to develop new inorganic–organic composite fibrous structure for realizing both high electromechanical coupling efficiency and mechanical property in the application of flexible sensors [41]. Piezoceramics with one-dimensional (1D) nanowire structure have more significant strain response than nanoparticles, which is conducive to stress transfer along the axial direction of the fiber and piezoelectric output when applied as highly-sensitive wearable sensor [42,43]. For wearable electronics composed of eco-friendly lead-free piezoelectric materials, $BaTiO_3$ fillers commonly exist in the form of nanoparticles [44]. Although the shape of $BaTiO_3$ nanorod/nanowire has been reported to enhance the piezoelectricity, the electrical output and sensitivity of the devices are poor and hard to be further improved based on structure due to the mismatch of physiochemical properties of different components and low degree of polarization [30,45].

Herein, and by taking into consideration the aforementioned problems, we have fabricated a fabric-based PENG for biomechanical sensing with ultra-high sensitivity and stability, in which high-aspect-ratio 1D $BaTiO_3$ nanowires (BTNW) with surface polydopamine (PDA) modification was incorporated into piezoelectric P(VDF-TrFE) fiber (PT) to form composite nanofiber (PT/pBTNW) *via* electrospinning technique for the first time (Scheme 1). We speculate that the bi-component of 1D BTNW and flexible piezoelectric P(VDF-TrFE) fibers, as well as the PDA effect of interfacial compatibility, which can exhibit hierarchical core–shell organo-inorganic structure for effectively perceiving external mechanical stress with a harmonious behavior, will generate flexible, mechanical-reinforced and highly piezoelectric fibers for improving sensing performance of PENG. The PDA nanolayer coated on the nanowires was conducted *via* a low-cost encapsulation process and assisted in improving dispersibility of the inorganic phase in the organic matrix with perfect organic–inorganic interfacial interaction. Through theoretical simulation and calculation, the hierarchically structural composite nanofibers and the interfacial enhancement exactly exhibit improved piezoelectric response and stress–strain response, which was instrumental in enhancing its wearability and sensing performance. Compared with the PENG made from neat P(VDF-TrFE) fibrous film, P(VDF-TrFE) fibrous film incorporating non-coated BTNW (PT/BTNW), and P(VDF-TrFE) fibrous film incorporating pBTNP (PDA-coated BTNP), the optimized PT/pBTNW-based PENG had higher sensing sensitivity and electrical signal outputs. Towards practical applications, the wearable and flexible piezoelectric sensor had rapid response time (~20.4 ms) and long-term durability after 9000 period cycles (<2.3 % decline) with a high sensitivity of 4.3 V N^{-1} under small force (<1.5 N). In addition, the PENG-based sensor could harvest multiple low and high-frequency mechanical signals of human body. We hope to pave a cost-effective way to develop high-performance and self-powered wearable bioelectronics for wearable bioelectronics in human biomechanical sensing.

2. Results and discussion

Fig. 1a displays the hydrothermal synthetic process of the $BaTiO_3$ nanowires (BTNW) and surface modification of the nanowires with polydopamine (PDA) *via in situ* polymerization of dopamine. For convenience, the resultant PDA-coated BTNW (PDA@BTNW) is abbreviated as pBTNW. The morphology of the obtained pBTNW was characterized by scanning electron microscopy (SEM) (Fig. 1b) and transmission electron microscopy (TEM) (Fig. 1c). From the TEM image, the PDA nanolayer with thickness of 18–25 nm uniformly wrapped the whole BTNW. The corresponding precursor $Na_2Ti_3O_7$ and $H_2Ti_3O_7$ nanowires had a statistical diameter of about 100 nm (Fig. S1). The average diameter of BTNW and pBTNW was ~ 232.1 ± 32.54 nm and 254.2 ±

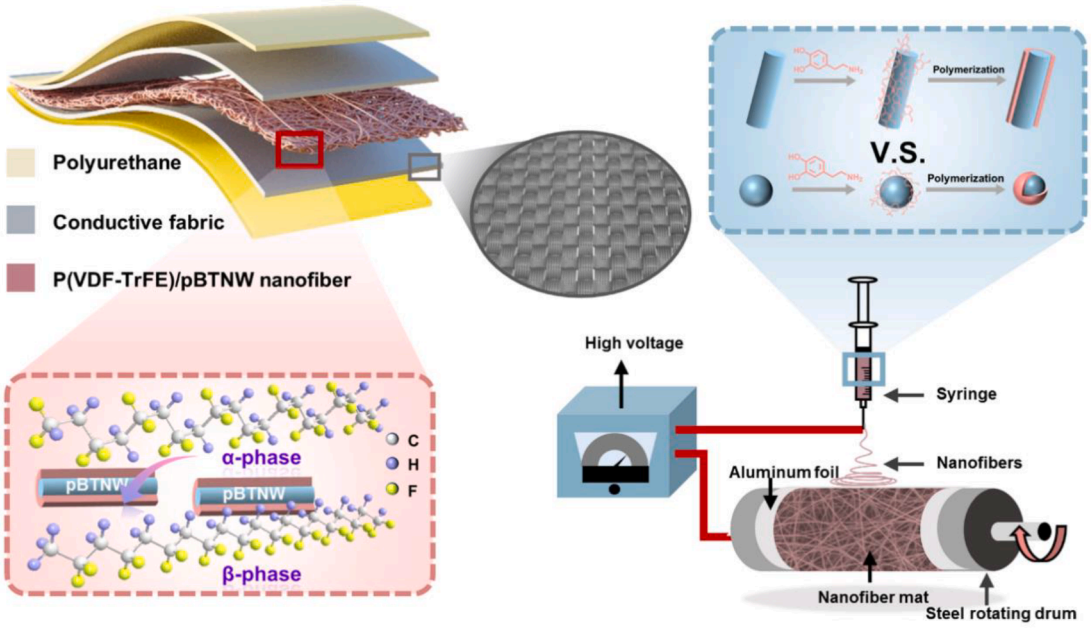

Scheme 1. Scheme of fabrication process and configuration of the composite fiber-based piezoelectric sensor and corresponding electrospinning apparatus.

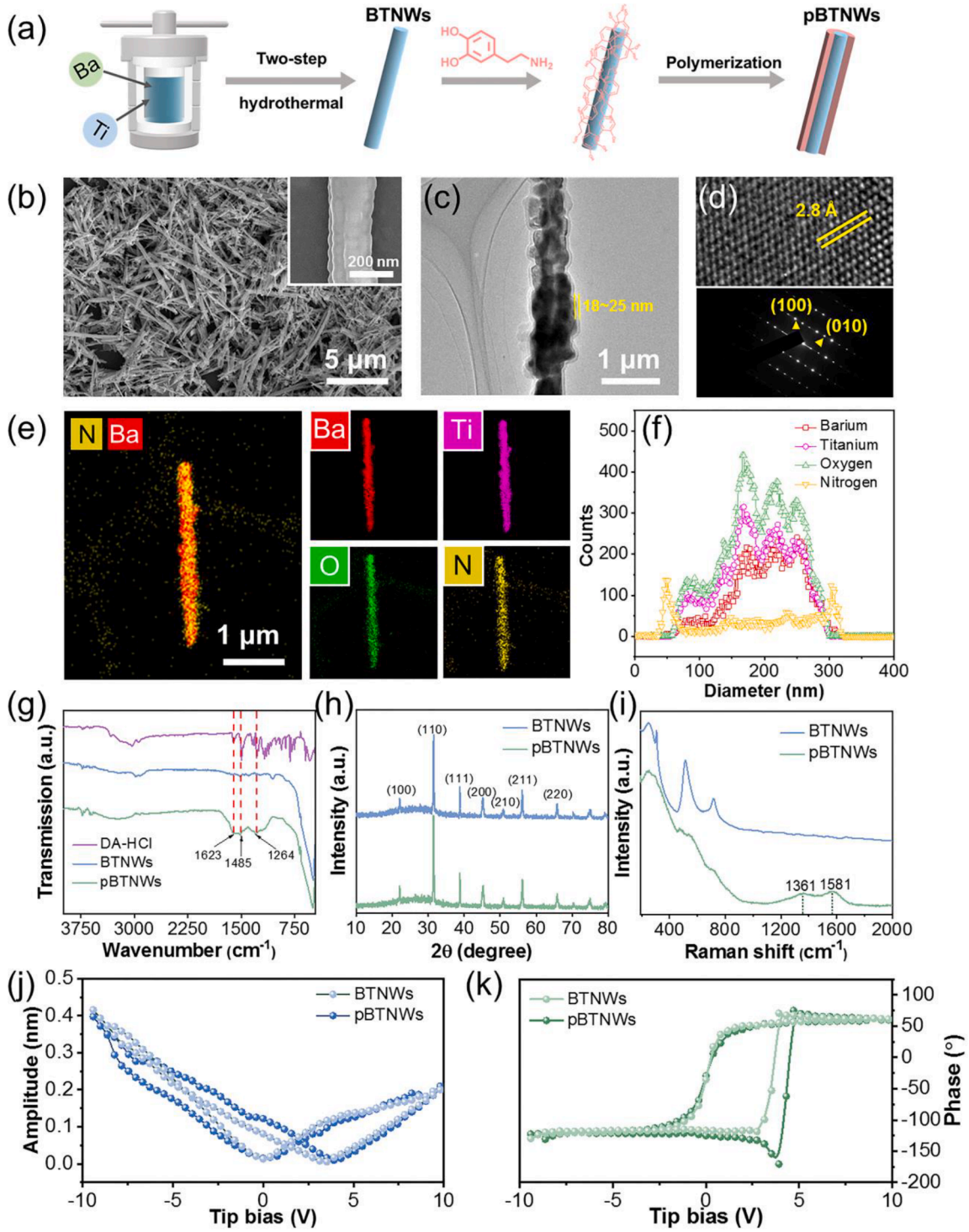

Fig. 1. Synthesis and structural characterization of pBTNW. (a) Synthetic scheme of pBTNW *via* two-step hydrothermal process and post-modification. (b) SEM, (c) TEM, (d) HRTEM (upper) and SAED (lower) images of pBTNW. Scale bar = 1 μm. (e) EDS mapping of Ba, Ti, O and N element on an individual nanowire. (f) EDS profiles of Ba, Ti, O, and N elements perpendicular to the length direction of one BTNW. (g) FT-IR spectra, (h) XRD patterns, and (i) Raman spectra of BTNW before and after PDA modification. Piezoresponse results of BTNW and pBTNW involving (j) amplitude butterfly-loop and (k) phase hysteresis curves.

45.78 nm, respectively, while their length was within the range of 3 ~ 3.78 μm, indicating a large aspect ratio about 15 (Fig. S2). From the high-resolution TEM (HRTEM) image and selected area electron diffraction (SAED) of pBTNW (Fig. 1d), the lattice spacing of 2.8 Å was in accordance with the (1 0 1) lattice plane of tetragonal $BaTiO_3$ (BTO) and the diffraction pattern suggested the single-crystal characteristic of the BTNW. These results implied the homogeneity of the obtained nanowires without obvious defect or impurity.

To visualize the element distribution, the two-dimensional and line-scan energy-dispersive spectrometer (EDS) element mapping were collected. As displayed in Fig. 1e, Ba, Ti, O and N were distributed throughout the nanowire. From the line-scan EDS, N element originated from PDA was mainly distributed in the shell area, verifying the successful coating of the PDA layer (Fig. 1f). In the Fourier transform infrared (FT-IR) spectrum for pBTNW, the peaks of 1264 cm^{-1}, 1485 cm^{-1} and 1623 cm^{-1} that corresponded to the modes of C—O, C—C

stretching vibration and N—H bending vibration, respectively, further proved the existence of PDA (Fig. 1g). Considering that the crystal structure of BTO determines its piezoelectricity, the crystal and phase structure of pBTNW were determined through X-ray diffraction (XRD) and Raman spectra. As shown in Fig. 1h, the XRD patterns of BTNW and pBTNW presented typical tetragonal perovskite structure without other phases. Moreover, the peak intensity of pBTNW was slightly higher than that of the BTNW, demonstrating that the introduction of PDA nanoshell did not change the crystalline structure of BTNW. In the Raman spectrum (Fig. 1i), the peaks at 250, 306, 513 and 718 cm^{-1} implied the existence of tetragonal phase BTNW [46], and the two bands at 1361 and 1581 cm^{-1} were attributed to the stretching of benzene ring in PDA [47,48].

Notably, the surface modification of BTNW with PDA significantly improved the dispersion stability of the nanowires in the electrospun DMF/acetone mixture (Fig. S3), which was expected to enhance the interfacial bonding between the nanowire filler and the polymer matrix. Compared with BTNW, the negative zeta potential of pBTNW was further reduced due to the positive PDA coating. As a reflection of variation in particle size, the polydispersity index (PDI) of pBTNW (0.097) was also decreased compared with that of BTNW (0.258), suggesting an improved dispersion of the modified nanowires (Fig. S4). It can be attributed to the potential chemical reaction between the hydroxy groups of BTNW and the phenol groups of PDA, thus contributing to the formation of benzene groups near the surface of BTNWs to partially inhibit aggregation [49]. Additionally, the grafted PDA layer is beneficial for mitigating surface energy of BTNWs, thereby increasing the interfacial compatibility with organic matrix [50,51].

Piezoelectric response of BTNW before and after PDA coating was evaluated by the piezoresponse force microscopy (PFM) measurement. To ensure the full contact between the samples and the PFM probe, nanowire with diameter of about 1 μm was specifically selected for the detection, and corresponding topography, amplitude and phase images were exhibited in Fig. S5. The maximum amplitude of the pBTNW reached 0.21 nm and 0.41 nm at the highest positive (+10 V) and negative (-10 V) tip bias, respectively, where the BTO dipoles were aligned along the direction of the electric field (Fig. 1j). And the calculated d_{33} coefficient of the BTNW and pBTNW reached 39 and 41 pm V^{-1}, respectively. The pBTNW showed a near 180° switching of the phase curve and larger hysteresis area than the uncoated BTNW, suggesting a higher local polarization (Fig. 1k). These results suggested that the pBTNW with a high aspect ratio and excellent dispersion presented good piezoelectricity. It was beneficial for the external loading transmission, which laid a vital foundation for the enhancement of the piezoelectric response and electromechanical conversion capability. Considering the possible impact of the aspect ratio of BTNW on its piezoelectricity, we selected two middle values of aspect ratios (AR) between the existing nanoparticles (AR = 1) and nanowires (AR = 15), and conducted simplified simulation and calculation to analyze their piezopotential differences under the same stress status. As shown in Fig. S6, the piezopotential increased with increased AR, and the highest potential reaches 0.79 V when the AR is 15, which may be associated with the enhanced stress conduction on the top and bottom surface of BTNWs. Future experimental studies involving the preparation and analysis of physiochemical properties on BTNWs with different aspect ratios would be necessary to further clarify the deep enhancement mechanism.

Electrospinning is regarded as a versatile method to prepare piezoelectric fibers with incremental β-phase benefit from the stretching force applied on the electrified liquid [52,53]. It has been found that the involved stretching and electric poling process can promote the alignment of dipoles in P(VDF-TrFE), thereby enhancing the piezoelectric sensitivity under an external stimulation. On the other hand, it is expected that the addition of the inorganic fillers will further help nucleation of the piezoelectric phase in the P(VDF-TrFE) [54]. Thereby, the composite nanofiber composed of P(VDF-TrFE) and pBTNW were fabricated through electrospinning. For convenience, the obtained composite films with consistent P(VDF-TrFE) contents and different pBTNW fractions of 0 wt%, 3 wt%, 5 wt%, 7 wt% and 10 wt% are denoted as PT/pBTNW-0, PT/pBTNW-3, PT/pBTNW-5, PT/pBTNW-7 and PT/pBTNW-10 nanofibers (NF), respectively. The SEM images of the fiber films with different pBTNW content (0–10 wt%) are displayed in Fig. 2a-e. The statistical results showed that the average diameter of the fibers slightly increased with the increased pBTNW contents from 768 ± 31.8 nm to 803 ± 19.08 nm, but without significant difference (Fig. S7). In addition, the thickness of all the fiber films was kept consistent by controlling the electrospinning time so as to eliminate the unwanted influence (Fig. S7f). From the SEM images, the bare BTNW without surface PDA modification were seriously agglomerated in the fiber matrix, which even punctuated the surface of the fiber when the mass fraction of BTNW reached 10 wt% (Fig. S8a). And the diameter of the fibers became more nonuniform, which might decrease the generation of piezoelectricity and weaken the feasibility of the prepared devices due to the possible crevices (Fig. S8b).

In contrast, the P(VDF-TrFE)/pBTNW nanofibers (PT/pBTNW NF) exhibited a smooth morphology free of bead and nanowire aggregation. The pBTNW was uniformly distributed in the P(VDF-TrFE) matrix and well-oriented along the extensive direction of the fiber (Fig. 2f, g). From the EDS element mapping (Fig. 2g), C and F element from polymer distributed in the whole fiber, while Ba, Ti, O and N elements from pBTNW located in the interior of the fiber. For comparison, P(VDF-TrFE)/pBTNP nanofibers (PT/pBTNP NF) incorporating pBTNP were prepared following the same nanoparticle surface modification and electrospinning process (Fig. S9-11). To illustrate the interaction between the pBTNW and the polymer matrix, XRD and Raman spectroscopy were conducted again. XRD spectra showed that the peak at $2\theta = 20.59°$ corresponding to the reflection from (110/200) crystal planes of β-phase became sharper as the pBTNW content increased (Fig. 2h). As shown in the enlarged image ranging from 18° to 26° (Fig. 2i), the peak area of β-phase extended with the increasing mass fraction of pBTNW, revealing the addition of pBTNW promoted the formation of β-phase in P(VDF-TrFE). In the Raman spectra (Fig. 2j), the band intensity of 840 cm^{-1} and 1430 cm^{-1} representing β-phase in P(VDF-TrFE) was strengthened with the increasing content of pBTNW. It might be attributed to the enhanced electrostatic interaction between –OH/–NH_2 in PDA and –CH_2/-CF_2 in P(VDF-TrFE) [14].

Differential scanning calorimetry (DSC) and FT-IR spectroscopy was used to quantify the crystallinity and β-phase of all the nanofiber samples. As shown in the DSC curves (Fig. 3a), the pBTNW content affected the thermal properties of the P(VDF-TrFE) nanofiber, as confirmed by the melting temperature peak shift of the nanofibers from 159.5 °C to 158.4 °C as the pBTNW content increased to 7 wt%. And the peak intensity remarkably enhanced with the content of pBTNW increased to 7 %, representing improved crystallinity in P(VDF-TrFE). The FT-IR spectra showed the typical characteristic peaks from β-phase at 840 cm^{-1}, 1290 cm^{-1} and 1430 cm^{-1} for all the samples, while the bands at 763 cm^{-1} and 976 cm^{-1} corresponding to the non-polar α-phase were not observable, validating the dominant presence of β-phase (Fig. 3b). Among all the samples, the PT/pBTNW-7 NF had the highest β-phase content (Table S1), which was also higher than the PT/pBTNP NF with equal BTNP mass fraction (7 wt%). It was noteworthy that the peaks at 882, 1123 and 1176 cm^{-1} of the PT/pBTNW NF shifted towards lower wavenumber relative to the neat P(VDF-TrFE) (Fig. S12). It can be ascribed to the formation of hydrogen bonds between –NH_2 groups in PDA and -CF- groups in P(VDF-TrFE) [55]. The crystallinity and β-phase content of P(VDF-TrFE) calculated from the DSC and FT-IR results showed that both crystallinity and β-phase content reached a highest value of 96.1 % when pBTNW mass fraction was 7 % (Fig. 3c). Appropriate content of the pBTNW in the P(VDF-TrFE) nanofibers could benefit crystallization of the polymer and act as a heterogeneous nucleating agent in polymeric matrix chains [56,57]. However, further increase of pBTNW mass fraction to 10 % induced decrease of β-phase.

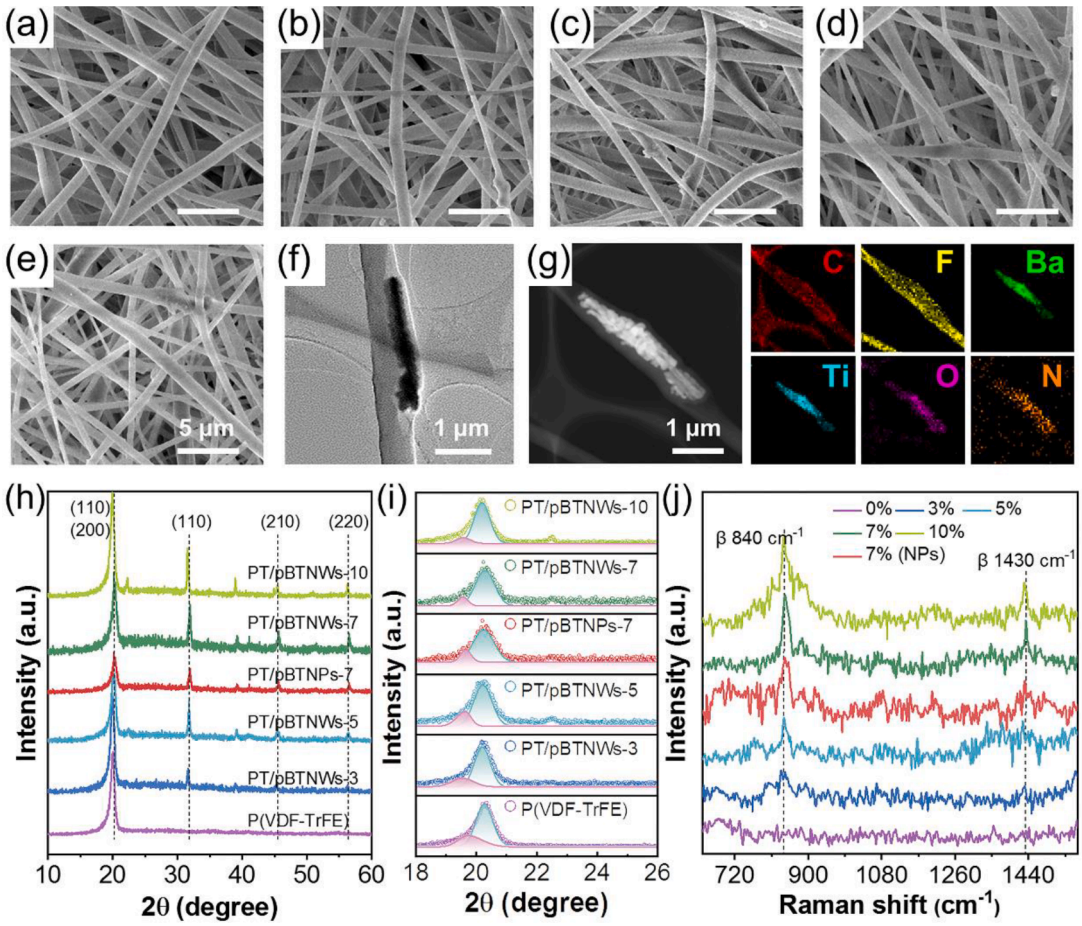

Fig. 2. Characterization of the electrospun composite films. SEM images of the as-synthesized fiber film with (a) PT/pBTNW-0 NF, (b) PT/pBTNW-3 NF, (c) PT/pBTNW-5 NF, (d) PT/pBTNW-7 NF and (e) PT/pBTNW-10 NF. Scale bar = 5 μm. (f) TEM and (g) dark field-TEM and EDS mapping of C, F, Ba, Ti, O, and N element in a single PT/pBTNW NF. Scale bar = 1 μm. (h) XRD patterns, (i) enlarged view of 18-26° from XRD pattern, and (j) Raman spectra of the composite fiber films with different mass fraction of pBTNW. As a control, the results of the fiber film with pBTNP were also shown.

The possible explanation to support this result might be that the increased defects caused from the high-loading pBTNW blocked the segmental motion as well as the alignment of the P(VDF-TrFE) chain and further hindered the segment from forming asymmetrical β-phase, and the great amount of β-phase might merge each other and form symmetrical α-phase, which resulted in the F(β) reduction to 86.9 % [58,59]. Moreover, in comparison with PT/pBTNP NF with equal BTNP mass fraction, PT/pBTNW NF possessed higher crystallinity and β-phase content. This was mainly attributed that the 1D nanowire structure well-aligned inside the fiber served as an enhanced nucleating agent, which might form more effective interaction with the flexible polymer matrix due to the more longitudinal shape than 0D nanoparticles.

The enhanced interaction can be further characterized by the X-ray photoelectron spectroscopy (XPS). The XPS survey spectra verified the existence of O and N elements from PDA in the composite fibers (Fig. 3d). The O 1 s peak was fitted into three photoelectron peaks at binding energy of 530.9, 532.2 and 533.55 eV, which corresponded to the oxygen element in BTNW, and C═O and C—O groups in PDA, respectively (Fig. 3e). From the deconvoluted N 1 s spectrum (Fig. 3f), the peaks at binding energy of 399.6 and 401.5 eV represented -N = and N—H in PDA. The corresponding XPS spectra of Ba and Ti element were shown in Fig. S13. After introducing the pBTNW into P(VDF-TrFE), the peak area of C-CF_2 and C-CF groups decreased accompanied by the increased peak area and intensity of -CF_2 group due to the strong interaction between –NH_2 in PDA and -CF_2 in P(VDF-TrFE) (Fig. 3g and S13d). These results clarified the covalent linking between BTNW and PDA through -C—O- bonding and the pBTNW showed strong intermolecular interactions with P(VDF-TrFE) to promote the dipole orientation [60]. Combined with the above DSC and FT-IR data, these results revealed that the PDA shell reinforced the interaction and compatibility at the organic–inorganic interface, and the addition of pBTNW acting as a nucleating enhancer promoted the self-alignment of P(VDF-TrFE) to oriented β-phase, as depicted in the schematic (Fig. 3h), which was expected to improve piezoelectricity of the composite fiber largely.

Considering the flexibility requirement of wearable sensors, mechanical properties of all the samples were characterized. Among all the samples, the PT/pBTNW NF displayed the best tensile strength with 42 % strain, suggesting higher mechanical properties than P(VDF-TrFE) and PT/pBTNP NF (Fig. 3i). The improvement in the mechanical properties is probably attributed to the good adhesion and the excellent coupling action of PDA, building up strong intermolecular forces exerted between the matrix and the PDA shell on BTNW [34,55]. From the tension stress–strain curves of the composite fibers, the Young's modulus of the PT/pBTNP film (25.08 MPa) was higher than the PT/pBTNW fiber film (21.16, 23.62, and 22.39 MPa for PT/pBTNW-3, PT/pBTNW-5, PT/pBTNW-7, respectively (inset, Fig. 3i). It was caused from the anisotropic structure of the nanowires and the PDA-promoted interfacial interaction and compatibility inside the fibers. Among all samples, the PT/pBTNW-10 exhibited the highest Young's modulus, which was attributed to the rich doping of BTNW crystal significantly increasing stiffness of polymer fibers, although in Fig. 3c the crystallinity of PT/pBTNW-10 decreased probably due to that the higher amount of PDA disrupted the crystallization of polymer. These results implied that

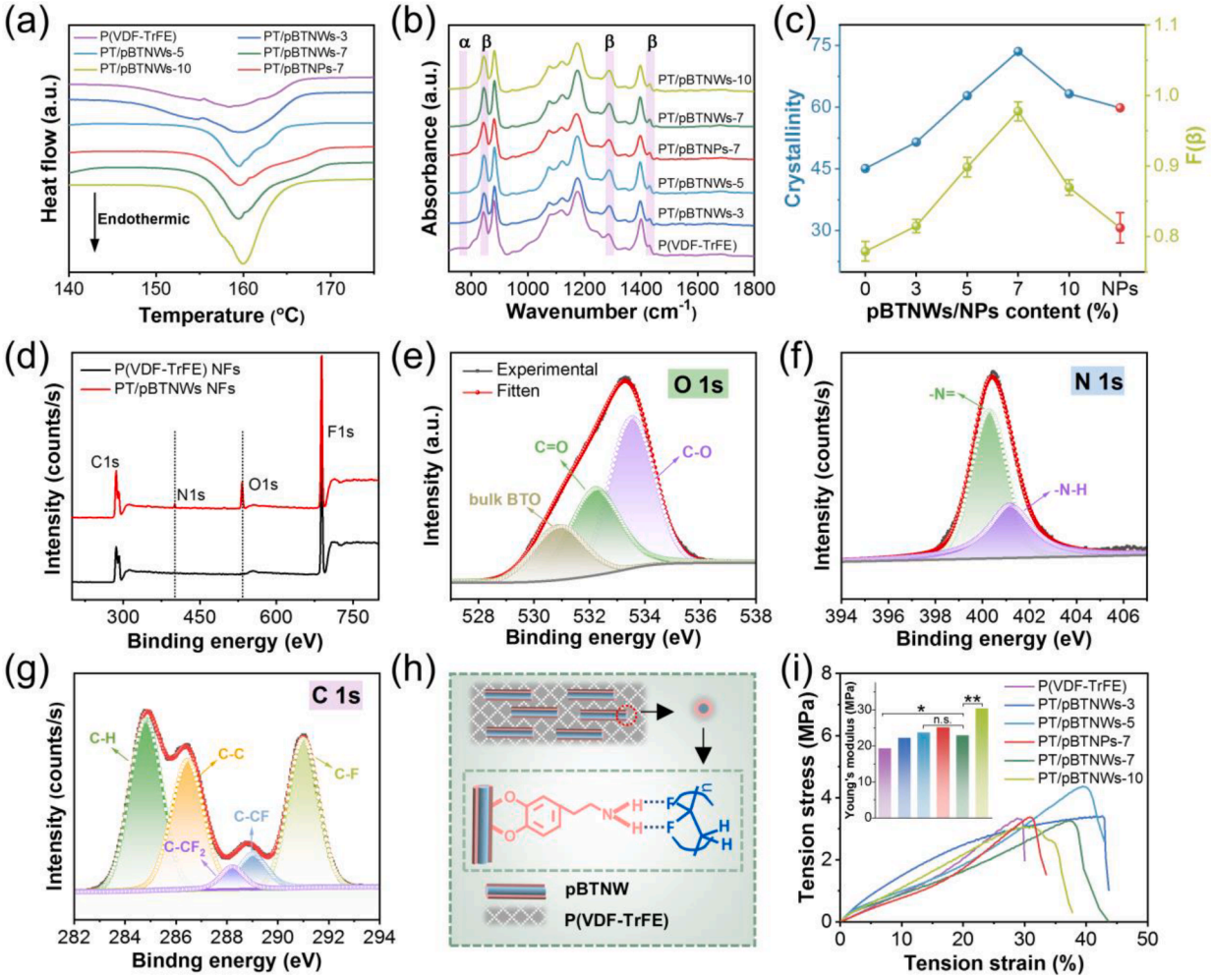

Fig. 3. Characterization of crystal phase and mechanical properties. (a) DSC thermograms and (b) FT-IR spectra of the neat P(VDF-TrFE) fiber film and composite fiber films. (c) The calculated crystallinity and β-phase contents (F_β) quantified from DSC curves and FT-IR spectra. (d) XPS survey spectra of neat P(VDF-TrFE) fiber and PT/pBTNW NF. (e) The O 1 s, (f) N 1 s of pBTNW and (g) C 1 s of PT/pBTNW NF. (h) Schematic of the interfacial interaction between P(VDF-TrFE) and pBTNW. (i) The tension stress–strain curves of the composite films. Inset shows the quantified Young's modulus acquired from the curves (n = 3, *** = $p < 0.001$, ** = $p < 0.01$).

the addition of the pBTNW into P(VDF-TrFE) matrix to form coaxial structure gave rise to the decreased Young's modulus as well as promoted the tensile strength compared with the typical nanoparticle doping. It will endow the final device with enhanced flexibility, stretchability, and be favorable to perceive external mechanical stress. However, too low Young's modulus was not beneficial for the device to resist external strains. Therefore, integrating the result of piezoelectricity, the PT/pBTNW-7 NF film was chosen as an optimized sample in following experiments.

The piezoelectric property as well as the presence of stable and switchable polarization of the composite fiber film PT/pBTNW-7 NF were verified through the PFM and P-E measurements. Fig. 4a-d show the corresponding topography, amplitude, phase and 3D topography image of PT/pBTNW-7 NF, in which the phase with high contrast matched well with the dark and bright region in the amplitude image, indicating the existence of polarization domains. The phase and amplitude butterfly-shaped curves are displayed in Fig. 4e. The maximum amplitude of the composite fiber film reached 7.07 nm and 7.25 nm at −10 V and + 10 V tip bias, respectively. The near 180° switch of the phase loop from −10 V to + 10 V was typical for the domains switching triggered by the external electric field. For comparison, we also conducted the PFM test on pristine P(VDF-TrFE) film as shown in Fig. S14. The maximum amplitude only reached 20 pm and 45 pm at the same tip bias, and the phase switch of positive and negative voltage was about 130°, reflecting a relatively weaker piezoresponse than the composite films (Fig. S14d). From the P-E hysteresis curves (Fig. 4f), the polarization switching appeared as the nonlinear ferroelectric hysteresis loop with the addition of pBTNWs and pBTNPs into P(VDF-TrFE) fibers. The value of remnant polarization (Pr) increased from 1.4 μC cm^{-2} of pure P(VDF-TrFE) fibers to 4.85 μC cm^{-2} of PT/pBTNWs-10. This result indicated that the polar axes of the randomly oriented grains was switched along the exogenous electric field of the same driving voltage, leading to the larger polarization with the increased doping of the incorporated pBTNWs into the polymer matrix. Notably, the control sample PT/pBTNP-7 (red dot line) exhibited lower Pr, proving the superiority of the nanowires than the nanoparticles on improving ferroelectricity, which was consistent with the above-mentioned analysis of crystal structure. In further evaluation of the piezoelectric coefficient (d_{33}) as a direct index reflecting piezoelectricity, it was found that the d_{33} value also increased with the increase of pBTNW content and reached the maximum of 34 pC N^{-1} for PT/pBTNW-7 (Fig. S14e).

To further reveal the mechanism of PDA modification on the promotion of organic–inorganic interface coupling, which strengthened the surface stress and brought forth excellent mechanical properties, finite element method (FEM) was used to simulate the response of PT/BTNW and PT/pBTNW using COMSOL Multiphysics [61]. The external load on

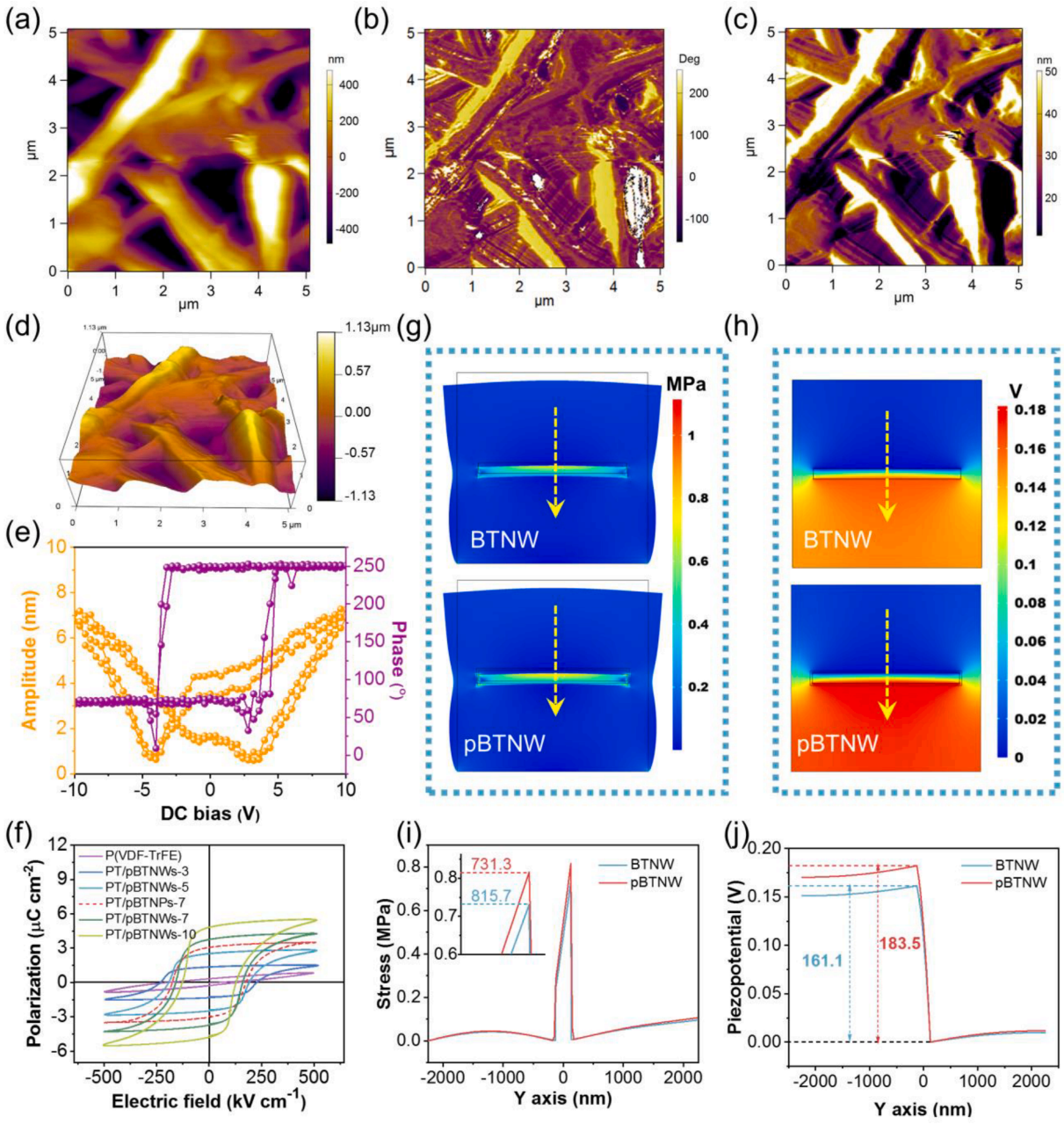

Fig. 4. Piezoresponse properties of the composite fibers. (a) Surface topography, (b) amplitude image, (c) phase image and (d) height information of PT/pBTNW NF. (e) The amplitude and hysteresis phase loop of the fiber under a tip bias from −10 to 10 V. (f) The ferroelectric hysteresis curve of different samples. COMSOL simulation of (g) stress and (h) corresponding piezopotential distribution of a single BTNW and pBTNW in the P(VDF-TrFE) matrix. (i) The stress and (j) corresponding piezopotential distribution derived along the direction of the yellow arrow in (g, h). (For interpretation of the references to color in this figure legend, the reader is referred to the web version of this article.)

the nanowire was considered as tensile strain under the bending condition, and thereby the nanowire would generate a tensile stress and corresponding piezopotential due to the bending impact (Fig. 4g, h). Owing to the obvious distinct Young's modulus of P(VDF-TrFE) and BTNW, the surface stress in the composite fibers for both PT/BTNW and PT/pBTNW is mostly concentrated on the inner BTNWs (Fig. 4g). As shown in the extracted line graph from the marked area (Fig. 4i), the induced stress on BTNW increases from 731.3 kPa to 815.7 kPa after PDA modification. Correspondingly, the enhanced stress increases the piezoelectric output of BTNW, and the potential differences increase from 161.1 mV to 183.5 mV (Fig. 4j). These results indicated that the PDA modification increased the stress distribution as well as the stress transfer, consequently leading to the optimized piezoelectric property of pBTNWs. To further clarify the mechanism on the BTNW-induced piezoelectricity enhancement compared with nanoparticles, COMSOL was also used to simulate the response of individual BTNW or BTNP. Fig. S15 depicts the piezopotential, stress, and displacement distribution of BTNP, BTNW, PT/BTNP, and PT/BTNW, respectively. The maximum piezoelectric potential under a bending force was calculated to be 0.78 V and 3.5 V for BTNW and PT/BTNW while the value for the BTNP and PT/BTNP was only 0.18 V and 1.32 V under the same condition (Fig. S15a-d, i). This difference was due to the higher mechanical tolerance, stress reinforcement within the fiber, and greater deformation of the nanowire (6.07 nm) than the nanoparticle (0.29 nm) (Fig. S15a-d, ii, iii). Through the simulation analysis from these two aspects, the modified PDA promoted interface interaction and stress transfer from P

(VDF-TrFE) to inner pBTNW, leading to the optimized piezoelectric output performance.

The piezoelectric output of the composite PT/pBTNW NF was systematically investigated. Fig. 5a displays the device design of the assembled piezoelectric nanogenerator (PENG). The five-layers device contained the middle layer of electrospun piezoelectric fiber film, two layers of conductive fabric as the top and bottom electrodes, and the flexible polyurethane (PU) films for encapsulation to protect the device from unpleasant environment or deconstruction. The whole thickness of the fabricated device was about 200 μm (Fig. S16a), and the morphology of the woven structure of conductive layers is displayed in Fig. S16b. it is evident that all layers are closely connected with each other. The optical picture shows the deformed device bent by a tweezer, indicating the flexibility suitable for wearable application. Fig. 5b elucidates the working principle of the PENG device during pressing and releasing movement. Initially, the dipoles maintain in an equilibrium state due to

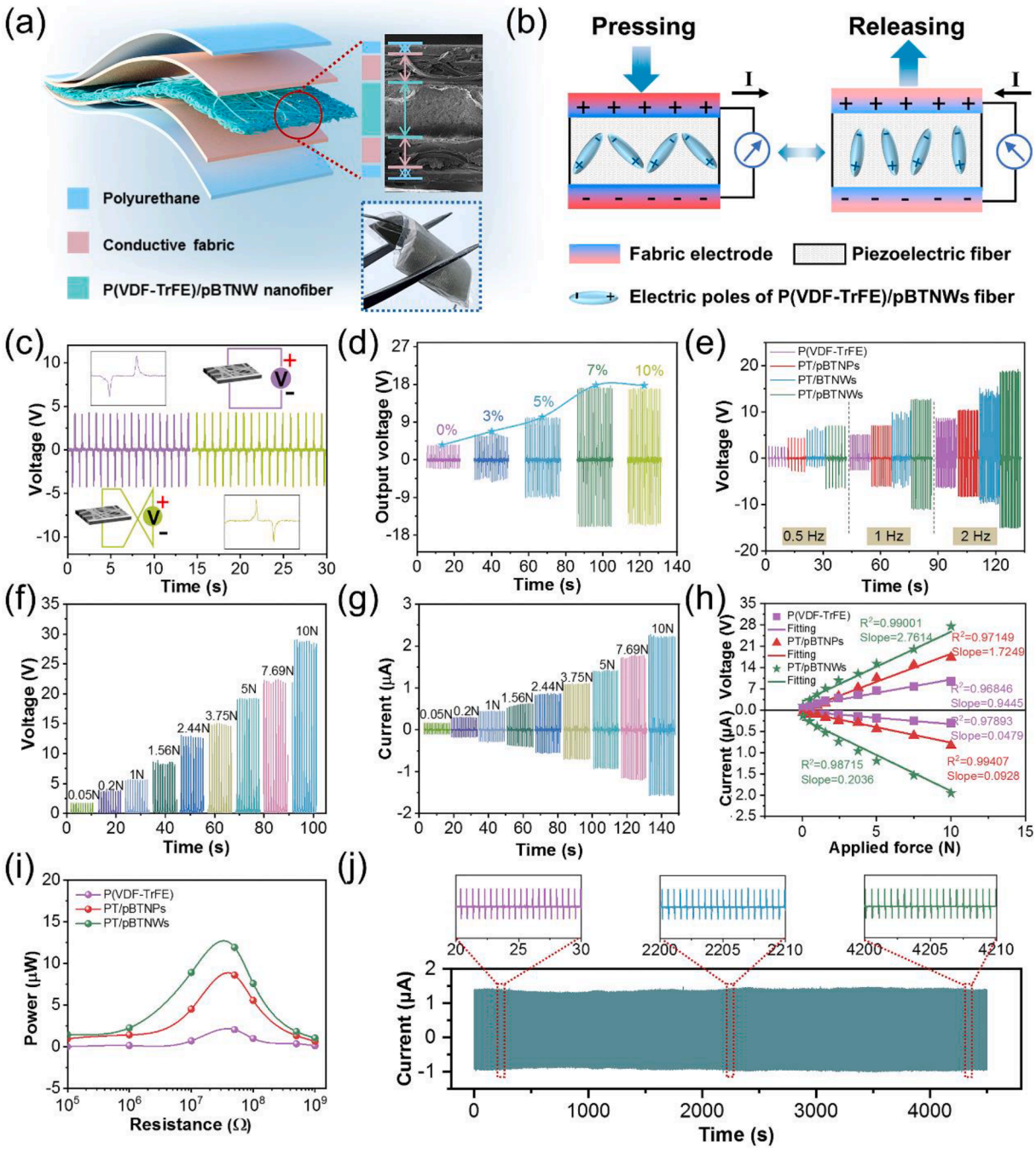

Fig. 5. Mechanism and analysis of the enhanced output performance. (a) Configuration design of the PENG and optical image of the device bent by a tweezer. The enlarged picture of the red circle region shows the cross-section SEM image of the whole device. (b) Working principle of piezoelectric output at an impacting/releasing mode. (c) Voltage output of the sensor with forward or reverse connection circuit. (d) Voltage output of the sensors at 1 Hz with different pBTNW mass fractions. (e) Comparison of the current output of the sensors based on P(VDF-TrFE) NF, PT/pBTNP-7 NF, PT/BTNW-7 NF and PT/pBTNW-7 NF at the frequencies of 0.5, 1 and 2 Hz under a constant pressure of 5 N. (f, g) Output performance of the sensor under the increasing impacted force after rectification. (h) Voltage and current output as a function of the applied forces at a range of 0–10 N. (i) The instantaneous output powers of the sensors on a series of external load resistances. (j) Durability evaluation under 9000 working cycles. (For interpretation of the references to color in this figure legend, the reader is referred to the web version of this article.)

that spontaneous polarization is constant [62]. When a continuous pressing force is subjected to the piezoelectric device, the electric dipoles oscillate and the negative and positive charges change in symmetry [63]. It results in decreased total polarization and increased dipole momentum, and the consequent charges/electrons flow through the external circuit, thus generating the electrical potential/current [52]. When the impacting force is withdrawn, the deformed device is gradually released, followed by generating an opposite electrical potential/current.

To clarify that the generated electrical signal upon external load was come from piezoresponse properties rather than electrostatic or triboelectric phenomenon, the switching polarity test was conducted by reversing the circuit connection mode (Fig. 5c and S17). Both voltage and current output were reversible due to the induced charges flowing back and forth, achieving a ~ 8 V and 0.6 μA piezoelectric output with the same pressing motions. It confirmed that the force-responsive output was indeed derived from the piezoelectric nature of the fiber film itself. To further exclude the possibility of artificial triboelectric signals, the electrical performance of the device composed of un-poled piezoelectric PT/pBTNW NF film was supplemented. As displayed in Fig. S18, it was evident that the voltage (~0.4 V) and current (~0.02 μA) output were considerably low compared with that of the poled one (Fig. 5c and S17). It was partly because that the internal electric dipoles were randomly aligned in the piezoelectric domain and led to almost no polarity without poling treatment. When subjected to a vertical pressure, the total polarization remained unchanged. Therefore, the piezopotential cannot be efficiently created, proving that the recorded electrical output of the PENG was attributed to the piezoelectric rather than triboelectric effect. Nevertheless, the generated electrical output was not zero, which might be attributed to the electrospinning-induced self-polarization. The voltage and current output performance of the PENG fabricated from different nanofiber film were detected under a periodic impacting/releasing motor. For the detection, the impacting force and frequency of displacement were constantly maintained at 5 N and 1 Hz, respectively. Exactly as expected, the PENG made from PT/pBTNW-7 NF presented both higher voltage and current than the neat P(VDF-TrFE) fibers (Fig. 5d and S19). With the mass fraction of pBTNW increased in the fibers, the output performance of the fabricated PENG device was correspondingly increased, which was resulted from the increased piezoelectricity of the composite fiber films. The values of voltage/current output for the devices increased from ~ 3.3 V/0.13 μA for neat P(VDF-TrFE) NF to the maximum of ~ 18.2 V/1.5 μA for the PT/pBTNW-7 NF. When the BTNW mass fraction was further increased to 10 wt%, the voltage output kept constant as that of 7 wt%, while the current output was slightly decreased. Moreover, in comparison with PT/pBTNP-7 NF-based PENG, the PT/pBTNW-7 NF-based PENG exhibited about 2.24- and 2.42-folds piezoelectric output for both voltage (18.2 V *v.s.* 7.5 V) and current (0.97 μA *v.s.* 0.4 μA), respectively (Fig. S20). Therefore, the PENG based on PT/pBTNW-7 NF was chosen for the following sensing applications.

The piezoelectric performance of the PENG devices was further investigated under different frequencies from 0.5 to 2 Hz, which represented the normal frequency range of human motion (Fig. 5e). The results revealed that the current output proportionally increased as the impact frequency increased, for all the PENG devices based on the neat P(VDF-TrFE) fiber film, and the composite ones with pBTNP, BTNW and pBTNW. To be specific, the voltage output of the PT/pBTNW NF-based PENG was increased from 6 V to 18.65 V with increasing impact frequency from 0.5 to 2 Hz, which was significantly higher than those from the BTNW, pBTNP and neat P(VDF-TrFE). Of note, the voltage peak shape and value of the PT/pBTNW NF-based PENG were consistent, suggesting that the piezoelectric sensor can satisfy the demand of repeatable human biomechanical sensing. In contrast, the voltage signals from the PT/BTNW NF-based PENG showed poor repeatability especially at the frequency of 1 Hz, which was mainly due to the insufficient organic–inorganic interfacial interaction without PDA modification (Fig. 5e). Response time of PENG is another essential basis for the assessment of a sensor. Upon finger impacting, the PT/pBTNW NF-based PENG had the shortest response time of 20.4 ms, in contrast to 64.9 ms, 70 ms and 115 ms for the PENGs based on PT/BTNW, PT/pBTNP, and neat P(VDF-TrFE), respectively (Fig. S21). It can be mainly attributed to that the addition of pBTNW induced more sensitive stress response that optimized stress and strain transfer, as depicted by simulation results, while the other devices exhibited longer response time due to the modulus mismatch at the two-phase interface and weaker stress-energy dissipation ability [64].

The voltage and current output were further recorded under a series of force from 0.05 to 10 N (Fig. 5f, g and S22). The result showed that the PENG can detect small force as low as 0.05 N, with an output of 1.73 V and 0.15 μA. According to the relationship between the applied force and the piezoelectric output, both the voltage and current values exhibited a good linear relationship with the applied forces (Fig. 5h). Through fitting and calculation, the PT/pBTNW NF-based PENG had a sensitivity of 2.76 V N^{-1} (equal to 6 kPa^{-1}) and linearity relevance (R^2) of 0.98 in the force range of 2.5–10 N. In comparison, in the same force range, the sensitivity of the PT/pBTNP NF and P(VDF-TrFE) NF-based PENGs was 1.72 V N^{-1} and 0.94 V N^{-1}, respectively (Fig. S23). However, the sensitivity of PT/pBTNW NF-based PENG was higher than 4.3 V N^{-1} (equal to 9.4 kPa^{-1}) when the force was lower than 1.5 N, which meant that the sensor device had an excellent mechano-electro relevance and a high sensitivity in the range of low forces (Fig. S23). In addition, the instantaneous electric power outputs of the three kinds of PENGs were compared (Fig. 5i and S24). The output of PT/pBTNW NF-based PENG reached 18.2 V and 1.56 μA with the maximum output power of 12.8 μW at a loading resistance of 50 MΩ, which was 1.47 and 5.85 times of the maximum output power of the PT/pBTNP NF and P(VDF-TrFE) NF-based PENG at the same loading resistance, respectively. The maximum instantaneous power density of the PT/pBTNW NF-based PENG was calculated to be 3.175 μW cm^{-2}. The load of the external circuit was the same as the internal impendence of the device, which was slightly lower than that of the PT/pBTNP NF and P(VDF-TrFE) NF-based PENGs, probably due to the enhanced induced charges transport at the organic–inorganic interface [20,21]. The potential use of PENG-based devices as power sources for wearable electronics has also been noticed [65]. To further investigate the energy harvesting property, capacitors (1.0, 3.3, or 4.7 μF) were connected to the PENG through a rectifier bridge and the corresponding charging curves were depicted in Fig. S25. The charging voltage of the 1.0, 3.3 and 4.7 μF capacitor reached 12.4, 6.7 and 2.9 V within 100 s, respectively, and the smaller capacitors obtained the larger charging rate. We compared the output performance of our optimized device with that reported in previous literatures, as listed in Table S2. The sensitivity and the maximum instantaneous power density in this work were superior to other PENGs with similar functional materials, suggesting that our optimized method is promising for enhancing the electrical performance of PENGs. Considering the practical application of wearable sensor in daily life, the PT/pBTNW NF-based PENG realized stable output after 9000 continuous pressing/releasing cycles, confirming the excellent stability of the sensor (Fig. 5j). Also, the output current (~1.5 μA) had almost no change during the 7-days-lasting test, suggesting the good stability and reliability (Fig. S26). For the wearable devices, it is necessary to investigate the waterproof performance, which is crucial for the long-term stability and feasibility of the device. After 5-days immersion in phosphate buffer saline (PBS) at room temperature, the PENG output performance showed no obvious weakening, and no liquid was penetrated into the PENG, indicating the good performance even in the liquid condition (Fig. S27).

The flexibility and excellent adaptability of the PENG sensor is advantageous as wearable sensor. The flexible sensor can be bended to up to 90°, for which the voltage output was in proportion to the bending angles (Fig. S28). Similarly, the reliable stability under bending status was also verified, which ensured the feasibility of the sensor upon

attached to different parts of body (Fig. S29). Based on the sensitive piezoelectric response, the optimized PENG composed of PT/BTNW-7 NF was applied for monitoring a series of human physiological movement (Fig. 6). For improving the comfort and adaptability of the sensor, the flexible device was attached directly on the skin by stretchable PU tape. The piezoelectric sensor was firstly mounted on elbow, wrist and knee, the three most representative human movement locations associated with joints (Fig. 6a-c). Obviously, the sensor did not generate any electrical output when the joints were straight forward. With the bending degree increasing gradually, the device went through an enhanced voltage output from ~ 0.2 V to 1.5 V for wrist, ~0.25 V to 3.58 V for elbow and ~ 1 V to 4 V for knee, respectively. Therefore, it can be applied for identifying the amplitude of the joint movement. The piezoelectric sensor can also distinguish the frequency of human motion. Fig. 6d presents the signal outputs generated by the sensor attached under the foot. The voltage output reached the maximum of 6.25 V under running, which was slightly higher than that under foot steeping (3.88 V). This difference in voltage output and frequency indicated the different instantaneous impacting stress and frequency. In addition to perceiving motions with large amplitude, the piezoelectric sensor can also perceive weak signals generated by subtle motions. Fig. 6e shows the electric output of a low-frequency gentle blink and a fast-forced blink when the flexible sensor was attached on the corner of the volunteer's eye. When the eyes blinked faster and stronger, the voltage output increased from 250 mV to 450 mV, demonstrating the fast response and high sensitivity of the sensor.

The sensing device was also fabricated into a data acquisition glove *via* integrating five independent sensors onto a nitrile glove. Fig. 6f and S30 shows that slight bending and strengthening movements of each finger were all precisely detected. Through Fast Fourier transform (FFT), the output voltage can easily discriminate the vibration of bending motion of each finger (Fig. 6g).

Distinct from the joint movement under relatively low frequencies, the ability of the PENG sensor as a proof-of-concept voice recognition device under high frequencies was explored using a loudspeaker as the sound wave source with multiple frequencies involving frequency range

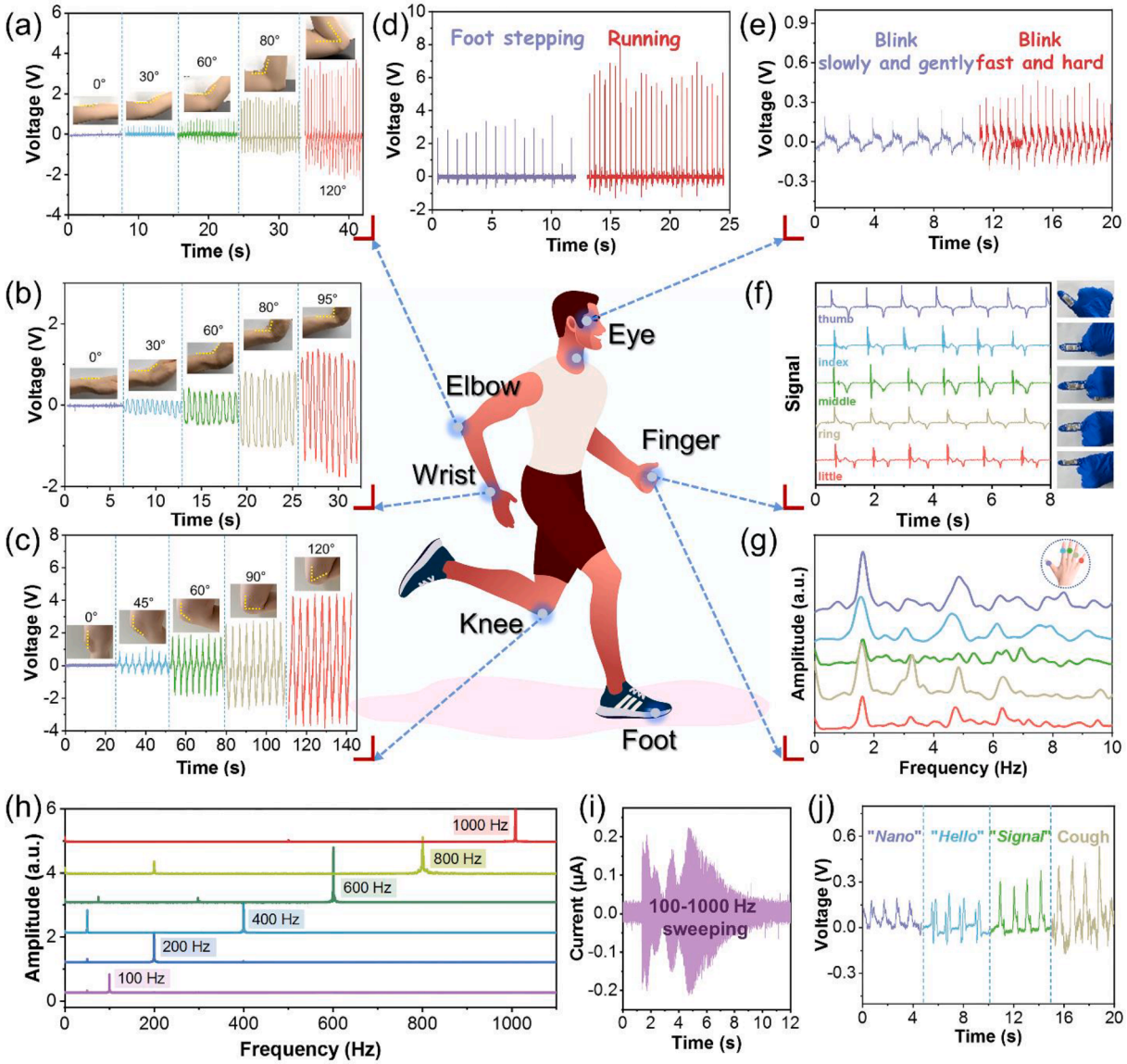

Fig. 6. Sensory performance of the device for physiological monitoring. (a-c) Perception of various joint motions of (a) elbow, (b) wrist, and (c) knee with different amplitudes. (d) Output signals of the sensor stimulated by foot stepping at different intensities and frequencies, and (e) blinking with different forces and frequencies. (f) Signals from the data acquisition glove with five independent sensors during bending motions of every finger and (g) respective FFT pattern. (h) The frequency spectra derived through Fast Fourier transform (FFT). (i) Electrical signal measured from the PENG sensor within sweeping frequencies of 100–1000 Hz. (j) Dynamic output for voice recognition when saying "*Nano*", "*Hello*" and "*Signal*", and vocal cords movement during coughing.

of human voices (100–1000 Hz) [66]. The voltage and current output of the PENG sensor first increased with vibration frequencies increasing from 100 Hz to 600 Hz, and then decreased with vibration frequencies further increasing from 600 Hz to 1000 Hz. It suggested the good mechano-electrical conversion performance in response to the high-frequency sound waves that contained the frequency of human voices (Fig. S31a, b). From the zoom-in views of the maximum voltage and current (Fig. S31c, d), it was found that the electrical outputs were basically stable under the external vibrations with constant frequency. Through FFT, the frequencies of the output signals were in line with the external frequencies (Fig. 6h), suggesting the response of PENG to the dynamic changes of frequencies. It can be observed that the current output of the sensor had different variations under the sweeping frequencies, and the maximum value was achieved at about 620 Hz, which might be the resonance frequency of the sensor (Fig. 6i). These results may promote us on implementing the applications of acoustic sensors and artificial cochlear [67]. Accordingly, the piezoelectric sensor was then attached on the neck of a volunteer. Considering that the when the volunteer spoke "*Nano*", "*Hello*" and "*Signal*", the distinguished piezoelectric signals were triggered by the vibration of the throat, matching the pronunciation characteristics of each word (Fig. 6j). The spoken words of "*Nano*" and "*Signal*" presented a disyllable pronunciation with a stress accent coming first. Thus, the sensor detected voltage profile contributed to a strong peak followed by a weak peak. In contrast, the voltage output showed different modes in pronouncing "*Hello*", of which the stress accent was located at the second syllable. In addition, a ~ 560 mV signal generated by the violent vibration in the process of coughing can also be accurately detected, which was higher than that of speaking calmly (~290 mV) (Fig. 6j). These signals were regular and stable, proving a satisfying reproducibility for sensing. All these results indicated that the PT/pBTNW NF-based piezoelectric sensor possessed excellent flexibility to perceive various human movements, and is sensitive to the environment changing including signal amplitude and frequency. It showed great potential especially in the remote control of human–machine interaction and internet of things [8,68].

3. Conclusion

In this work, we have successfully integrated PDA-modified BTNW into polymeric P(VDF-TrFE) matrix to form highly flexible and piezoelectric nanofiber with coaxial and hierarchical architecture *via* electrospinning process. The PDA nanolayer coated on BTNW acted as an effective interfacial connector between the P(VDF-TrFE) polymer and anisotropic BTNW, thus reinforcing the stress transference through the interfacial interaction and promoting the piezoelectric output. The piezoelectric PENG composed of PT/pBTNW-7 NF achieved a maximum output of 18.2 V, 1.5 μA and output power of 12.8 μW, which were 2.24, 2.42 and 1.47 times of the PENG based on equivalent BTNP. Its flexibility can match well with human skin to meet the need of future wearable device. As a wearable and self-powered sensor, the piezoelectric sensor can sensitively detect various human physiological motions such as joint movement and eyes blinking with different strength and frequency. Also, the short response time (20.4 ms) enables the sensor to precisely recognize the voice pronunciation. We wish this work can propose a cost-efficient approach to develop high sensitivity and performance sensors which displays great potentials in personalized healthcare and remotely controlling of human–machine interaction interface, and deepening the basic understanding of the mechanism of piezoelectric composites.

4. Experimental section

4.1. Materials

Tris-base and dopamine hydrochloride (DA-HCl) were supplied by Sigma-Aldrich. Titanium dioxide powders (TiO_2, 99 %, anatase), barium hydroxide octahydrate ($Ba(OH)_2{\cdot}8H_2O$, ACS, 98 %), N, *N*-dimethyl formamide (DMF), and acetone were purchased from Macklin (Shanghai, China). Poly (vinylidenefluoride-*co*-trifluoroethylene) (P(VDF-TrFE), 75/25 mol%) was purchased from Piezotech (Piezotech, ARKEMA, France). The other reagents and chemicals were all purchased from Peking Reagent (Beijing, China) and used directly without further treatment.

4.2. Synthesis of $BaTiO_3$ nanowires (BTNW)

The BTNW were synthesized using a two-step hydrothermal reaction as previously reported with a slight modification [36,69]. 3 g TiO_2 powder was mixed with 60 mL sodium hydroxide (NaOH) aqueous solution (10 M), magnetically stirred for 18 h, and then sealed in a 100 mL Teflon-line stainless autoclave. After being heated at 210 °C for 24 h, the $Na_2Ti_3O_7$ nanowires were obtained. Subsequently, the $Na_2Ti_3O_7$ nanowires were soaked in an aqueous 0.2 M HCl solution for 24 h with slow stirring to produce $H_2Ti_3O_7$ nanowires, which acted as the precursor crystals for the synthesis of BTNW. In the second step, the obtained $H_2Ti_3O_7$ nanowires were dispersed in 60 mL $Ba(OH)_2{\cdot}8H_2O$ aqueous solution with a molar ratio of Ba:Ti = 2:1, and stirred for 24 h. Then, the mixed solution was transferred into a 100 mL Teflon-autoclave and kept at 200 °C for 85 min. The resultant BTNW were dispersed in 0.2 M HCl, washed with deionized water and ethanol subsequently, and dried at 80 °C for further experiments. $BaTiO_3$ nanoparticles (BTNP) as the control sample were synthesized as reported previously [70].

4.3. Preparation of PDA@BTNW (pBTNW)

The surface modification of BTNW was performed based on the in-situ polymerization of dopamine (DA) into polydopamine (PDA). 1 g BTNW were added into Tris-HCl buffer solution (10 mM, pH 8.5) and ultrasonically treated for 30 min. Then, DA-HCl (0.2 g mL^{-1}) was dissolved in the BTNW suspension and magnetically stirred at 60 °C for 12 h in the air. Afterward, the suspension was centrifugated and washed with ethanol until the supernatant became colorless, followed by drying at 60 °C. The color of BTNW powders after polydopamine (PDA) modification was change to dark brown due to the dopamine polymerization. The PDA@BTNP was synthesized in a similar way. For short, the resultant PDA@BTNW and PDA@BTNP were abbreviated as pBTNW and pBTNP, respectively.

4.4. Fabrication of electrospun piezoelectric nanofibers

P(VDF-TrFE) powders with 20 wt% concentration was first dissolved in 3:2 (v/v) DMF/acetone mixture (10 mL) by magnetically stirring for 12 h at room temperature. Subsequently, the pBTNW with mass fraction of 0 wt%, 3 wt%, 5 wt%, 7 wt% and 10 wt% was dispersed in the polymer solution by ultrasonication for 30 min and stirred for 3 h at 50 °C. For comparison, the P(VDF-TrFE) solution with pBTNP was also prepared. Electrospinning process was performed by loading 3 mL of the mixed solution into a 5 mL plastic syringe fitted with a 21 G stainless steel nozzle. A high voltage supply was set to 18 kV between the nozzle tip and the collector at a distance of 15 cm. An aluminum foil was covered on the drum rotator, of which the roller speed was selected to be 500 rpm for collecting the fibers. The solution was delivered at a flow rate of 1 mL h^{-1} at the humidity of 45 % under the atmosphere temperature. All the electrospun films were obtained under the above-mentioned conditions for 4 h.

4.5. Configuration of the fiber sensor

The piezoelectric fiber-based sensor was fabricated with the fiber film, two conductive fabric electrodes and two package layers. Specifically, the as-electrospun fiber films were cut into desired dimension (2.3 cm × 2.3 cm) and two conductive fabric tapes (2 cm × 2 cm) were

attached to both sides of the fiber film as the electrodes. And the copper strips were pasted on the surface of the electrodes acting as the test leads. Then, the obtained sandwiched configuration was encapsulated with polyimide tapes. For collecting biomechanical signals, the sensor was sealed with medical tape to make it fit better with human skin. Finally, the whole device was subjected to an appropriate compression, which helped to avoid the generation of triboelectric signal by eliminating the gap between different layers. Informed consent was received from the volunteer driving the PENG.

4.6. Characterizations and measurements

The morphologies of all the samples were recorded by a field emission scanning electron microscope (SEM, Nova, NanoSEM, 450, USA) and transmission electron microscopy (TEM, JEM-2100, JEOL, Japan). The images of high-resolution TEM (HRTEM), selected-area electron diffraction (SAED) pattern and energy-dispersive X-ray (EDX) mapping were characterized using JEM-2100F (JEOL, Japan). The size distribution of the samples was determined by the Image J software. The crystalline structures were analyzed *via* X-ray diffraction (XRD, PANalytical ltd., Netherland) equipped with Cu K_α radiation and Raman spectroscopy (LabRam HR evolution, Jobin Yvon, France). The Fourier-transform infrared (FT-IR) spectra were performed on a Veraex80V (Bruner Corp., USA) within the range of 400–4000 cm^{-1}. The crystallinity of the electrospun fibers was determined by differential scanning calorimetry (DSC, DSC8500, PerkinElmer, USA) in a nitrogen atmosphere with the heating rate of 10 °C min^{-1} and temperature ranging from 50 to 200 °C. Chemical modification of all the samples was evaluated by X-ray photoelectron spectroscopy (XPS, EscaLab 250Xi, Thermo Fisher Inc., USA). The thickness of all the fiber films was determined using a digital thickness gauge (YHT780, China) by putting the film sample between two fixtures. The surface morphology and piezoelectric properties of the nanowires and fibers were characterized with a piezoresponse force microscopy (PFM, MFP-3D-SA, Asylum Research, USA) using a contact mode. The tensile performance of the fibers was investigated by a universal testing machine (Instron EP3000, USA). The P-E hysteresis curves were measured by a ferroelectric test setup (RTI-MultiFerroic, USA). Electrical outputs of the packaged devices were measured by Keithley 6514 electrometer and the corresponding data were recorded by Labview software.

4.7. Calculations and simulations

Calculation of β-phase of P(VDF-TrFE): The FT-IR spectra of all the samples were used to quantify the proportion of β-phase (F(β)) of P(VDF-TrFE) by the Equation (1):

$$F(\beta) = \frac{A_\beta}{1.27A_\alpha + A_\beta} \#(1)$$

Where A_α and A_β suggest the absorbance values at 763 cm^{-1} and 840 cm^{-1}, respectively [57]. And the factor of 1.27 is calculated by dividing the absorption coefficients at these two wavenumbers.

Calculation of crystallinity of P(VDF-TrFE): The degree of crystallinity (χ_c) is obtained by the Equation (2):

$$\chi_c = \left\{ \frac{\Delta H_f}{\Delta H_f^0 \times \left(1 - \frac{filler(wt\%)}{100}\right)} \right\} \times 100\% \#(2)$$

Where ΔH_f is the measured fusion enthalpy, and ΔH_f^0 is the enthalpy of P(VDF-TrFE) with 100 % crystalline (45 J g^{-1}) [71]. The filler (wt%) represents the weight percentage of the inorganic filler. The calculation results of F(β) and χ_c are shown in Table S1.

4.8. COMSOL simulation

The simulation was conducted through a three-dimensional analysis *via* COMSOL Multiphysics software. For the simulation of BTNW and pBTNW, one side of the nanowire was fixed and grounded while the other side was set as suspended potential. When simulating the stress distribution of the nanowire, a pair of opposite tensile strains were exerted on the left and right ends of the P(VDF-TrFE) matrix, and the bottom was fixed. For the simulation of inorganic ceramics within the P(VDF-TrFE) matrix, the constructed model consisted of a cubic BTNP or an anisotropic BTNW, both with a 25 nm-thickness PDA shell. For simplification, the model of the composite fiber consisted of a P(VDF-TrFE) fiber with 750 nm width and 10 μm length. For pBTNP, the polarization was aligned with the global co-ordinate z-axis, while the bottom was fixed and grounded. For pBTNW, the polarization was perpendicular to the length direction. It was assumed that the analog impact force on the nanomaterials is 10 N. The other material parameters used in this simulation, such as density, elasticity matrix (*cE*), coupling matrix (*eES*) and relative permittivity (ε_r) of P(VDF-TrFE), $BaTiO_3$ and polydopamine are from COMSOL Multiphysics.

4.9. Statistics analysis

Statistical significance of all the data was performed by measuring one-way analysis of variance (ANOVA analysis) using the GraphPad Software. The results are presented as the average ± standard deviation (mean ± SD). To statistically analyze and evaluate significant differences between elected treatments, Turkey's multiple comparison tests were utilized. The sampling size (the time of replicates) was three. Differences were statistically significant at $p < 0.05$ with the significance levels of $^*p < 0.05$, $^{**}p < 0.01$, and $^{***}p < 0.001$.

Declaration of Competing Interest

The authors declare that they have no known competing financial interests or personal relationships that could have appeared to influence the work reported in this paper.

Data availability

Data will be made available on request.

Acknowledgments

The work was supported by the National Key R&D project from Minister of Science and Technology, China (2016YFA0202703), the National Nature Science Foundation (No. 81471784), and the Nature Science Foundation of Beijing (2172058), the Fundamental Research Funds for the Central Universities (E2EG6802X2), and the National Youth Talent Support Program.

Appendix A. Supplementary data

Supplementary data to this article can be found online at https://doi.org/10.1016/j.cej.2022.139077.

References

[1] C. Shi, Z. Zou, Z. Lei, P. Zhu, W. Zhang, J., Xiao, Heterogeneous integration of rigid, soft, and liquid materials for self-healable, recyclable, and reconfigurable wearable electronics, Sci Adv 6 (45) (2020), https://doi.org/10.1126/sciadv.abd0202.

[2] Y.S. Choi, R.T. Yin, A. Pfenniger, J. Koo, R. Avila, K. Benjamin Lee, S.W. Chen, G. Lee, G. Li, Y. Qiao, A. Murillo-Berlioz, A. Kiss, S. Han, S.M. Lee, C. Li, Z. Xie, Y.-Y. Chen, A. Burrell, B. Geist, H. Jeong, J. Kim, H.-J. Yoon, A. Banks, S.-K. Kang, Z. J. Zhang, C.R. Haney, A.V. Sahakian, D. Johnson, T. Efimova, Y. Huang, G. D. Trachiotis, B.P. Knight, R.K. Arora, I.R. Efimov, J.A. Rogers, Fully implantable and bioresorbable cardiac pacemakers without leads or batteries, Nat Biotechnol 39 (10) (2021) 1228–1238.

[3] F.R. Fan, W. Tang, Z.L. Wang, Flexible Nanogenerators for Energy Harvesting and Self-Powered Electronics, Adv Mater 28 (22) (2016) 4283–4305, https://doi.org/10.1002/adma.201504299.

[4] S. Park, S.W. Heo, W. Lee, D. Inoue, Z. Jiang, K. Yu, H. Jinno, D. Hashizume, M. Sekino, T. Yokota, K. Fukuda, K. Tajima, T. Someya, Self-powered ultra-flexible electronics via nano-grating-patterned organic photovoltaics, Nature 561 (7724) (2018) 516–521, https://doi.org/10.1038/s41586-018-0536-x.

[5] Z.L. Wang, J. Song, Piezoelectric nanogenerators based on zinc oxide nanowire arrays, Science 312 (5771) (2006) 242–246, https://doi.org/10.1126/science.1124005.

[6] L. Gu, N. Cui, L. Cheng, Q. Xu, S. Bai, M. Yuan, W. Wu, J. Liu, Y. Zhao, F. Ma, Y. Qin, Z.L. Wang, Flexible fiber nanogenerator with 209 V output voltage directly powers a light-emitting diode, Nano Lett 13 (1) (2013) 91–94, https://doi.org/10.1021/nl303539c.

[7] Y. Su, C. Chen, H. Pan, Y.e. Yang, G. Chen, X. Zhao, W. Li, Q. Gong, G. Xie, Y. Zhou, S. Zhang, H. Tai, Y. Jiang, J. Chen, Muscle Fibers Inspired High-Performance Piezoelectric Textiles for Wearable Physiological Monitoring, Advanced Functional Materials 31 (19) (2021) 2010962.

[8] W. Deng, T. Yang, L. Jin, C. Yan, H. Huang, X. Chu, Z. Wang, D. Xiong, G. Tian, Y. Gao, H. Zhang, W. Yang, Cowpea-structured PVDF/ZnO nanofibers based flexible self-powered piezoelectric bending motion sensor towards remote control of gestures, Nano Energy 55 (2019) 516–525, https://doi.org/10.1016/j.nanoen.2018.10.049.

[9] F. Mokhtari, J. Foroughi, T. Zheng, Z. Cheng, G.M. Spinks, Triaxial braided piezo fiber energy harvesters for self-powered wearable technologies, Journal of Materials Chemistry A 7 (14) (2019) 8245–8257, https://doi.org/10.1039/c8ta10964h.

[10] Z. Li, Z.L. Wang, Air/Liquid-pressure and heartbeat-driven flexible fiber nanogenerators as a micro/nano-power source or diagnostic sensor, Adv Mater 23 (1) (2011) 84–89, https://doi.org/10.1002/adma.201003161.

[11] K. Dong, X. Peng, Z.L. Wang, Fiber/Fabric-Based Piezoelectric and Triboelectric Nanogenerators for Flexible/Stretchable and Wearable Electronics and Artificial Intelligence, Adv Mater 32 (5) (2020) e1902549.

[12] J.H. Han, K.M. Bae, S.K. Hong, H. Park, J.-H. Kwak, H.S. Wang, D.J. Joe, J.H. Park, Y.H. Jung, S. Hur, C.D. Yoo, K.J. Lee, Machine learning-based self-powered acoustic sensor for speaker recognition, Nano Energy 53 (2018) 658–665, https://doi.org/10.1016/j.nanoen.2018.09.030.

[13] L. Ma, R. Wu, A. Patil, S. Zhu, Z. Meng, H. Meng, C. Hou, Y. Zhang, Q. Liu, R. Yu, J. Wang, N. Lin, X.Y. Liu, Full-Textile Wireless Flexible Humidity Sensor for Human Physiological Monitoring, Advanced Functional Materials 29 (43) (2019) 1904549.

[14] T. Li, M. Qu, C. Carlos, L. Gu, F. Jin, T. Yuan, X. Wu, J. Xiao, T. Wang, W. Dong, X. Wang, Z.-Q. Feng, High-Performance Poly(vinylidene difluoride)/Dopamine Core/Shell Piezoelectric Nanofiber and Its Application for Biomedical Sensors, Advanced Materials 33 (3) (2021) 2006093.

[15] Y. Zhang, L. Zhou, X. Gao, C. Liu, H. Chen, H. Zheng, J. Gui, C. Sun, L. Yu, S. Guo, Performance-enhanced flexible piezoelectric nanogenerator via layer-by-layer assembly for self-powered vagal neuromodulation, Nano Energy 89 (2021) 106319.

[16] K. Kapat, Q.T.H. Shubhra, M. Zhou, S. Leeuwenburgh, Piezoelectric Nano-Biomaterials for Biomedicine and Tissue Regeneration, Advanced Functional Materials 30 (44) (2020) 1909045.

[17] C. Peter, H. Kliem, Ferroelectric imprint and polarization in the amorphous phase in P(VDF-TrFE), Journal of Applied Physics 125 (17) (2019) 174107.

[18] J. Hafner, S. Benaglia, F. Richheimer, M. Teuschel, F.J. Maier, A. Werner, S. Wood, D. Platz, M. Schneider, K. Hradil, F.A. Castro, R. Garcia, U. Schmid, Multi-scale characterisation of a ferroelectric polymer reveals the emergence of a morphological phase transition driven by temperature, Nature, Communications 12 (1) (2021), https://doi.org/10.1038/s41467-020-20407-6.

[19] S.D.B. Sreeja, S. Gopalan, C.O. Sreekala, Piezoelectric studies of PEDOT:PSS incorporated BaTiO3/ PDMS micro-generator, Materials Today: Proceedings 33 (2020) 1379–1383, https://doi.org/10.1016/j.matpr.2020.05.042.

[20] W. Zhai, J. Nie, L. Zhu, Enhanced Flexible Poly(vinylidene fluoride-trifluorethylene) Piezoelectric Nanogenerators by SnSe Nanosheet Doping and Solvent Treatment, ACS Appl Mater Interfaces 13 (27) (2021) 32278–32285, https://doi.org/10.1021/acsami.1c08347.

[21] X. Guan, B. Xu, J. Gong, Hierarchically architected polydopamine modified BaTiO3@P(VDF-TrFE) nanocomposite fiber mats for flexible piezoelectric nanogenerators and self-powered sensors, Nano Energy 70 (2020) 104516.

[22] Q.i. Xu, J. Wen, Y. Qin, Development and outlook of high output piezoelectric nanogenerators, Nano Energy 86 (2021) 106080.

[23] J. Kim, M. Jang, G. Jeong, S. Yu, J. Park, Y. Lee, S. Cho, J. Yeom, Y. Lee, A. Choe, Y.-R. Kim, Y. Yoon, S.S. Lee, K.-S. An, H. Ko, MXene-enhanced β-phase crystallization in ferroelectric porous composites for highly-sensitive dynamic force sensors, Nano Energy 89 (2021) 106409.

[24] X. Yuan, X. Gao, X. Shen, J. Yang, Z. Li, S. Dong, A 3D-printed, alternatively tilt-polarized PVDF-TrFE polymer with enhanced piezoelectric effect for self-powered sensor application, Nano Energy 85 (2021) 105985.

[25] S.R.A. Ruth, V.R. Feig, H. Tran, Z., Bao, Microengineering Pressure Sensor Active Layers for Improved Performance, Advanced Functional Materials 30 (39) (2020), https://doi.org/10.1002/adfm.202003491.

[26] B.Y. Lee, D.H. Kim, J. Park, K.I. Park, K.J. Lee, C.K. Jeong, Modulation of surface physics and chemistry in triboelectric energy harvesting technologies, Sci Technol Adv Mater 20 (1) (2019) 758–773, https://doi.org/10.1080/14686996.2019.1631716.

[27] C. Wang, Y. Zhang, B. Zhang, B. Wang, J. Zhang, L.Q. Chen, Q. Zhang, Z.L. Wang, K. Ren, Flexophotovoltaic Effect in Potassium Sodium Niobate/Poly(Vinylidene Fluoride-Trifluoroethylene) Nanocomposite, Adv Sci (Weinh) 8 (8) (2021) 2004554, https://doi.org/10.1002/advs.202004554.

[28] P. Chen, P. Wu, X. Wan, Q. Wang, C. Xu, M. Yang, J. Feng, B. Hu, Z. Luo, Ultrasound-driven electrical stimulation of peripheral nerves based on implantable piezoelectric thin film nanogenerators, Nano Energy 86 (2021) 106123.

[29] M. Xie, Y. Zhang, M.J. Krasny, C. Bowen, H. Khanbareh, N. Gathercole, Flexible and active self-powered pressure, shear sensors based on freeze casting ceramic-polymer composites, Energy Environ Sci 11 (10) (2018) 2919–2927, https://doi.org/10.1039/c8ee01551a.

[30] M. Zhu, M. Lou, I. Abdalla, J. Yu, Z. Li, B. Ding, Highly shape adaptive fiber based electronic skin for sensitive joint motion monitoring and tactile sensing, Nano Energy 69 (2020) 104429.

[31] W. Tong, Q. An, Z. Wang, Y. Li, Q. Tong, H. Li, Y. Zhang, Y. Zhang, Enhanced Electricity Generation and Tunable Preservation in Porous Polymeric Materials via Coupled Piezoelectric and Dielectric Processes, Adv Mater 32 (39) (2020) e2003087.

[32] S. Sharma, A. Chhetry, M. Sharifuzzaman, H. Yoon, J.Y. Park, Wearable Capacitive Pressure Sensor Based on MXene Composite Nanofibrous Scaffolds for Reliable Human Physiological Signal Acquisition, ACS Appl Mater Interfaces 12 (19) (2020) 22212–22224, https://doi.org/10.1021/acsami.0c05819.

[33] Y. Fu, H. He, T. Zhao, Y. Dai, W. Han, J. Ma, L. Xing, Y. Zhang, X. Xue, A Self-Powered Breath Analyzer Based on PANI/PVDF Piezo-Gas-Sensing Arrays for Potential Diagnostics Application, Nanomicro Lett 10 (4) (2018) 76, https://doi.org/10.1007/s40820-018-0228-y.

[34] Z. Wang, T. Wang, C. Wang, Y. Xiao, P. Jing, Y. Cui, Y. Pu, Poly(vinylidene fluoride) Flexible Nanocomposite Films with Dopamine-Coated Giant Dielectric Ceramic Nanopowders, Ba(Fe 0.5 Ta 0.5)O 3 , for High Energy-Storage Density at Low Electric Field, ACS Appl. Mater. Interfaces 9 (34) (2017) 29130–29139.

[35] J. Jiang, S. Tu, R. Fu, J. Li, F. Hu, B. Yan, Y. Gu, S. Chen, Flexible Piezoelectric Pressure Tactile Sensor Based on Electrospun BaTiO3/Poly(vinylidene fluoride) Nanocomposite Membrane, ACS Appl Mater Interfaces 12 (30) (2020) 33989–33998, https://doi.org/10.1021/acsami.0c08560.

[36] C.K. Jeong, C. Baek, A.I. Kingon, K.I. Park, S.H. Kim, Lead-Free Perovskite Nanowire-Employed Piezopolymer for Highly Efficient Flexible Nanocomposite Energy Harvester, Small 14 (19) (2018) e1704022.

[37] X. Du, Y. Liu, J. Wang, H. Niu, Z. Yuan, S. Zhao, X. Zhang, R. Cao, Y. Yin, N. Li, C. Zhang, Y. Xing, W. Xu, C. Li, Improved Triboelectric Nanogenerator Output Performance through Polymer Nanocomposites Filled with Core-shell-Structured Particles, ACS Appl Mater Interfaces 10 (30) (2018) 25683–25688, https://doi.org/10.1021/acsami.8b05966.

[38] Y.P. Su, L.N. Sim, H.G.L. Coster, T.H. Chong, Incorporation of barium titanate nanoparticles in piezoelectric PVDF membrane, Journal of Membrane Science 640 (2021) 119861.

[39] S. Liu, J. Zhai, Improving the dielectric constant and energy density of poly (vinylidene fluoride) composites induced by surface-modified SrTiO3 nanofibers by polyvinylpyrrolidone, Journal of Materials Chemistry A 3 (4) (2015) 1511–1517, https://doi.org/10.1039/c4ta04455j.

[40] A. Maliakal, H. Katz, P.M. Cotts, S. Subramoney, P. Mirau, Inorganic oxide core, polymer shell nanocomposite as a high K gate dielectric for flexible electronics applications, J Am Chem Soc 127 (42) (2005) 14655–14662, https://doi.org/10.1021/ja052035a.

[41] J. Wu, N. Qin, D. Bao, Effective enhancement of piezocatalytic activity of BaTiO3 nanowires under ultrasonic vibration, Nano Energy 45 (2018) 44–51, https://doi.org/10.1016/j.nanoen.2017.12.034.

[42] M.H. Seo, S.J. Choi, S.H. Park, J.Y. Yoo, S.K. Lim, J.S. Lee, K.W. Choi, M.S. Jo, I. D. Kim, J.B. Yoon, Material-Independent Nanotransfer onto a Flexible Substrate Using Mechanical-Interlocking Structure, ACS Nano 12 (5) (2018) 4387–4397, https://doi.org/10.1021/acsnano.8b00159.

[43] Q. Wang, J. Li, Y. Lei, Y. Wen, Z. Wang, X. Zhan, F. Wang, F. Wang, Y. Huang, K. Xu, J. He, Oriented Growth of Pb1- x Snx Te Nanowire Arrays for Integration of Flexible Infrared Detectors, Adv Mater 28 (18) (2016) 3596–3601, https://doi.org/10.1002/adma.201506338.

[44] Y. Zhang, H. Kim, Q. Wang, W. Jo, A.I. Kingon, S.-H. Kim, C.K. Jeong, Progress in lead-free piezoelectric nanofiller materials and related composite nanogenerator devices, Nanoscale Advances 2 (8) (2020) 3131–3149, https://doi.org/10.1039/c9na00809h.

[45] B. Zhao, Z. Chen, Z. Cheng, S. Wang, T. Yu, W. Yang, Y. Li, Piezoelectric Nanogenerators Based on Electrospun PVDF-Coated Mats Composed of Multilayer Polymer-Coated BaTiO3 Nanowires, ACS Applied Nano Materials 5 (6) (2022) 8417–8428, https://doi.org/10.1021/acsanm.2c01538.

[46] J. Wu, Q. Xu, E. Lin, B. Yuan, N. Qin, S.K. Thatikonda, D. Bao, Insights into the Role of Ferroelectric Polarization in Piezocatalysis of Nanocrystalline BaTiO3, ACS Appl Mater Interfaces 10 (21) (2018) 17842–17849, https://doi.org/10.1021/acsami.8b01991.

[47] J.-J. Feng, P.-P. Zhang, A.-J. Wang, Q.-C. Liao, J.-L. Xi, J.-R. Chen, One-step synthesis of monodisperse polydopamine-coated silver core–shell nanostructures for enhanced photocatalysis, New J. Chem. 36 (1) (2012) 148–154, https://doi.org/10.1039/c1nj20850k.

[48] C. Shuai, G. Liu, Y. Yang, F. Qi, S. Peng, W. Yang, C. He, G. Wang, G. Qian, A strawberry-like Ag-decorated barium titanate enhances piezoelectric and antibacterial activities of polymer scaffold, Nano Energy 74 (2020) 104825.

[49] A. Mayeen, K. M. s., M.S. Jayalakshmy, S. Thomas, D. Rouxel, J. Philip, R. N. Bhowmik, N. Kalarikkal, Dopamine functionalization of BaTiO 3 : an effective strategy for the enhancement of electrical, magnetoelectric and thermal properties of BaTiO 3 -PVDF-TrFE nanocomposites, Dalton Trans. 47 (6) (2018) 2039–2051.

[50] H.-C. Yang, R.Z. Waldman, M.-B. Wu, J. Hou, L. Chen, S.B. Darling, Z.-K. Xu, Dopamine: Just the Right Medicine for Membranes, Advanced Functional Materials 28 (8) (2018) 1705327.
[51] Y. Liu, K. Ai, L. Lu, Polydopamine and its derivative materials: synthesis and promising applications in energy, environmental, and biomedical fields, Chem Rev 114 (9) (2014) 5057–5115, https://doi.org/10.1021/cr400407a.
[52] Y.M. Yousry, K. Yao, A.M. Mohamed, W.H. Liew, S. Chen, S. Ramakrishna, Theoretical Model and Outstanding Performance from Constructive Piezoelectric and Triboelectric Mechanism in Electrospun PVDF Fiber Film, Advanced Functional Materials 30 (25) (2020) 1910592.
[53] X. Wan, Y. Zhao, Z. Li, L. Li, Emerging polymeric electrospun fibers: From structural diversity to application in flexible bioelectronics and tissue engineering, Exploration 2 (1) (2022) 20210029.
[54] L. Persano, C. Dagdeviren, C. Maruccio, L. De Lorenzis, D. Pisignano, Cooperativity in the enhanced piezoelectric response of polymer nanowires, Adv Mater 26 (45) (2014) 7574–7580, https://doi.org/10.1002/adma.201403169.
[55] Y. Xie, Y. Yu, Y. Feng, W. Jiang, Z. Zhang, Fabrication of Stretchable Nanocomposites with High Energy Density and Low Loss from Cross-Linked PVDF Filled with Poly(dopamine) Encapsulated BaTiO3, ACS Appl Mater Interfaces 9 (3) (2017) 2995–3005, https://doi.org/10.1021/acsami.6b14166.
[56] L. Wan, W. Tian, N. Li, D. Chen, Q. Xu, H. Li, J. He, J. Lu, Hydrophilic porous PVDF membrane embedded with BaTiO3 featuring controlled oxygen vacancies for piezocatalytic water cleaning, Nano Energy 94 (2022) 106930.
[57] L. He, J. Lu, C. Han, X. Liu, J. Liu, C. Zhang, Electrohydrodynamic Pulling Consolidated High-Efficiency 3D Printing to Architect Unusual Self-Polarized beta-PVDF Arrays for Advanced Piezoelectric Sensing, Small 18 (15) (2022) e2200114.
[58] P. Hu, L. Yan, C. Zhao, Y. Zhang, J. Niu, Double-layer structured PVDF nanocomposite film designed for flexible nanogenerator exhibiting enhanced piezoelectric output and mechanical property, Composites Science and Technology 168 (2018) 327–335, https://doi.org/10.1016/j.compscitech.2018.10.021.
[59] T. Bhatta, S. Sharma, K. Shrestha, Y. Shin, S. Seonu, S. Lee, D. Kim, M. d. Sharifuzzaman, SM.S. Rana, J.Y. Park, Siloxene/PVDF Composite Nanofibrous Membrane for High-Performance Triboelectric Nanogenerator and Self-Powered Static and Dynamic Pressure Sensing Applications, Advanced Functional Materials 32 (25) (2022) 2202145.
[60] C. Shuai, G. Liu, Y. Yang, W. Yang, C. He, G. Wang, Z. Liu, F. Qi, S. Peng, Functionalized BaTiO3 enhances piezoelectric effect towards cell response of bone scaffold, Colloids Surf B Biointerfaces 185 (2020), 110587, https://doi.org/10.1016/j.colsurfb.2019.110587.
[61] X. Zhou, S. Wu, C. Li, F. Yan, H. Bai, B.o. Shen, H. Zeng, J. Zhai, Piezophototronic effect in enhancing charge carrier separation and transfer in ZnO/BaTiO3 heterostructures for high-efficiency catalytic oxidation, Nano Energy 66 (2019) 104127.
[62] K. Zhang, S. Wang, Y.a. Yang, A One-Structure-Based Piezo-Tribo-Pyro-Photoelectric Effects Coupled Nanogenerator for Simultaneously Scavenging Mechanical, Thermal, and Solar Energies, Advanced Energy Materials 7 (6) (2017) 1601852.
[63] X. Huang, Q. Qin, X. Wang, H. Xiang, J. Zheng, Y. Lu, C. Lv, K. Wu, L. Yan, N. Wang, C. Xia, Z.L. Wang, Piezoelectric Nanogenerator for Highly Sensitive and Synchronous Multi-Stimuli Sensing, ACS Nano 15 (12) (2021) 19783–19792, https://doi.org/10.1021/acsnano.1c07236.
[64] X. Huang, Y. Wang, X. Zhang, Ultrarobust, hierarchically anisotropic structured piezoelectric nanogenerators for self-powered sensing, Nano Energy 99 (2022) 107379.
[65] M.B. Khan, D.H. Kim, J.H. Han, H. Saif, H. Lee, Y. Lee, M. Kim, E. Jang, S.K. Hong, D.J. Joe, T.-I. Lee, T.-S. Kim, K.J. Lee, Y. Lee, Performance improvement of flexible piezoelectric energy harvester for irregular human motion with energy extraction enhancement circuit, Nano Energy 58 (2019) 211–219, https://doi.org/10.1016/j.nanoen.2019.01.049.
[66] F. Chen, Y. Wu, Z. Ding, X. Xia, S. Li, H. Zheng, C. Diao, G. Yue, Y. Zi, A novel triboelectric nanogenerator based on electrospun polyvinylidene fluoride nanofibers for effective acoustic energy harvesting and self-powered multifunctional sensing, Nano Energy 56 (2019) 241–251, https://doi.org/10.1016/j.nanoen.2018.11.041.
[67] J.H. Han, J.-H. Kwak, D.J. Joe, S.K. Hong, H.S. Wang, J.H. Park, S. Hur, K.J. Lee, Basilar membrane-inspired self-powered acoustic sensor enabled by highly sensitive multi tunable frequency band, Nano Energy 53 (2018) 198–205, https://doi.org/10.1016/j.nanoen.2018.08.053.
[68] S.K. Ghosh, P. Adhikary, S. Jana, A. Biswas, V. Sencadas, S.D. Gupta, B. Tudu, D. Mandal, Electrospun gelatin nanofiber based self-powered bio-e-skin for health care monitoring, Nano Energy 36 (2017) 166–175, https://doi.org/10.1016/j.nanoen.2017.04.028.
[69] H. Tang, Y. Lin, H.A. Sodano, Synthesis of High Aspect Ratio BaTiO3Nanowires for High Energy Density Nanocomposite Capacitors, Advanced Energy Materials 3 (4) (2013) 451–456, https://doi.org/10.1002/aenm.201200808.
[70] X. Wan, X. Zhang, Z. Liu, J. Zhang, Z. Li, Z.L. Wang, L. Li, Noninvasive manipulation of cell adhesion for cell harvesting with piezoelectric composite film, Applied Materials Today 25 (2021) 101218.
[71] S. Wang, H.-Q. Shao, Y. Liu, C.-Y. Tang, X. Zhao, K. Ke, R.-Y. Bao, M.-B. Yang, W. Yang, Boosting piezoelectric response of PVDF-TrFE via MXene for self-powered linear pressure sensor, Composites Science and Technology 202 (2021) 108600.